

Submitted to ApJ, 29 October 2001; in original form 30 June 2001

## Broad and shifted iron-group emission lines in $\gamma$ -ray bursts as tests of the hypernova scenario

G. C. McLaughlin, R. A. M. J. Wijers, G. E. Brown

*Department of Physics and Astronomy, State University of New York, Stony Brook, NY  
11794-3800*

`gail@tonic.physics.sunysb.edu`, `rwijers@mail.astro.sunysb.edu`,  
`epopenoe@nuclear.physics.sunysb.edu`

and

H. A. Bethe

*Floyd R. Newman Laboratory of Nuclear Studies, Cornell University, Ithaca, NY 14853,  
USA*

### ABSTRACT

In the hypernova/collapsar model of  $\gamma$ -ray bursts, it is natural that radiation is emitted by the inner engine for some time after the burst. This has been discussed as a possible source of the X-ray line emission observed in some afterglows. We show here that the natural geometry of a hypernova –a source of radiation at the bottom of a deep funnel– has very significant consequences for the shape and central energy of the observed emission lines: the lines acquire a very broad scattering wing on the low-energy side and a characteristic second peak one Compton wavelength away from the initial energy, due to the once- and twice-scattered photons. We suggest that this explains the large width of the observed lines. Furthermore, the downscattering lowers the central line energy (by up to 1 keV in the source rest frame, before the lines become unrecognizable), so that the observed line energies can become consistent with originating from cobalt and nickel, as expected in few-day-old supernova ejecta.

*Subject headings:* gamma rays: bursts — supernovae — line: profiles — radiative transfer

## 1. Introduction

The discovery of  $\gamma$ -ray burst afterglows in X-ray (Costa et al. 1997), optical (van Paradijs et al. 1997), and radio (Frail et al. 1997) wavelengths greatly increased the possibilities for studying the objects emitting this radiation. This quickly led to the first measurement of a redshift (Metzger et al. 1997) and the realization that the relativistic fireball-blastwave model for their nature (Rees and Mészáros 1992; Mészáros and Rees 1997) explained the afterglows very well (Wijers et al. 1997). (For recent reviews, see Van Paradijs, Kouveliotou, and Wijers 2000 and Piran 1999.) The phenomenal inferred emitted energy is at least that of a supernova; together with rapidly variable  $\gamma$ -ray emission this suggests a stellar-remnant origin. Leading candidates of this type are mergers of neutron stars and/or black holes (Eichler et al. 1989; Mochkovitch et al. 1993; Janka et al. 1999; Salmonson et al. 2001) or core collapses of massive stars (Woosley 1993; Paczyński 1998). The latter are gaining favor for long  $\gamma$ -ray bursts (duration over 2 s (Kouveliotou et al. 1993); these are the only ones for which afterglows have been found), for a number of reasons: (i) Some GRBs have shown evidence of association with a supernova, either by a clear supernova found in their error box (GRB 980425/SN 1998bw; Galama et al. 1998), or by late-time afterglow light curves showing a feature consistent with a supernova. Clearest among the latter are GRB 980326 (Bloom et al. 1999a) and GRB 970228 (Reichart 1999; Galama et al. 2000), though other less clear cases have been claimed. Given the relative rarity of these cases and the difficulty of detecting a supernova in the presence of a bright afterglow, it is unclear whether this association holds more generally. (ii) The small spatial offsets between  $\gamma$ -ray burst counterparts and their host galaxies (e.g., Bulik et al. 1999; Bloom et al. 1999b, 2000) are hard to reconcile with merging neutron stars, given their high expected space velocities and long merger times, which should have them merge far away from where they were born. (iii) The X-ray column density and extinction, as well as the prevalence of strong MgI absorption lines in many optical spectra of afterglows, indicate that  $\gamma$ -ray bursts often occur in dense regions and behind much larger column densities than expected from random locations in galaxies (Galama and Wijers 2001). This suggests they occur amidst the large amounts of dust and gas one expects to find in star forming regions. (iv) There is increasing evidence that  $\gamma$ -ray bursts are associated with star formation on a more global scale, both because the  $\gamma$ -ray burst rate as a function of redshift is consistent with following the star formation rate (Totani 1997; Wijers et al. 1998; Krumholz et al. 1998; Kommers et al. 2000; Schmidt 2001) and because the average star formation rate in  $\gamma$ -ray burst host galaxies is significantly above that of samples of galaxies at the same redshift (Fruchter 2001).

An emission line has recently been found in some X-ray afterglows of  $\gamma$ -ray bursts (Piro et al. 1999; Antonelli et al. 2000; Piro et al. 2000), whose energy is roughly consistent with Fe  $K\alpha$  at the redshift of the host. This line has been adduced as evidence that the environment

of the burst is heavily enriched in iron, and thus the result of a recent supernova explosion. If this interpretation is correct, it would provide strong support for the connection between  $\gamma$ -ray bursts and stellar explosions. This makes the lines of considerable importance to unveiling the nature of  $\gamma$ -ray bursts. In this paper, we investigate some problems with the interpretation of the lines, and suggest a mechanism that may help solve them. We begin by discussing models for the formation of iron group lines in  $\gamma$ -ray burst afterglows and their difficulties in accounting for all the observations (sect. 2). Then we discuss our model for electron scattering of line photons in a hypernova funnel (sect. 3) and the types of emission line profile that it predicts (sect. 4). Finally, we discuss the relevance of our findings to current and future observations and some possible complications (sect. 5) and summarize our conclusions (sect. 6).

## 2. Motivation

The general thrust of models for the X-ray lines is that X rays from the burst or afterglow irradiate cooler material, ionizing it almost completely. Recombination of the material causes emission lines, and around 6–8 keV the iron group elements are the dominant contributors. The very large iron line luminosity, about  $10^{52}(\text{d}\Omega/4\pi)$  photons/s, sustained for a day or so, requires  $10^{57}(\text{d}\Omega/4\pi)$  emitted photons ( $\text{d}\Omega$  is the solid angle illuminated by the iron-line source). If every atom emitted only once (e.g., if the ionization happened in a flash, and every atom recombined only once, or if the recombination time were of order the observed emission time), one would need of order  $50(\text{d}\Omega/4\pi)M_{\odot}$  of pure iron group material to take part. Therefore, one needs a dense enough medium to have many recombinations per atom, but even then detailed models often require the presence of large amounts of this material. This gives rise to the claim that the irradiated medium is heavily enriched in iron, and thus must have been enriched by a supernova quite recently. The reported BeppoSAX WFC discovery of a transient absorption feature in the prompt burst spectrum of GRB 990705 (Amati et al. 2000) would, if typical of hypernovae, also set stringent constraints on the amount of enriched ejecta and their distance from the  $\gamma$ -ray burst.

The models for the origin of the line come in two basic kinds. In one type of model, the supranova, the medium is a shell ejected in an explosion some months prior to the  $\gamma$ -ray burst (Vietri et al. 2001). When the burst flux hits the shell it emits its lines; as one needs many photons per atom, the recombination time should be much less than the burst duration, so the density needs to be high. However, the observed duration of the line emission, about a day, is much longer. One can get this by choosing the shell size to be about a light day, so that the duration of the emission is set by the light crossing time of the shell. The emission

is naturally isotropic, so  $10^{57}$  line photons must be produced. Weak points of this model are a few: first, the observed supernova ‘bumps’ in  $\gamma$ -ray burst afterglow light curves are consistent with the supernova going off at the same time as the  $\gamma$ -ray burst, rather than the required few months before the burst. Second, the required time delay is created by having a supernova first make a massive neutron star which is partly supported by rotation. When it slows down, its centrifugal support gives way at some point and it collapses to a black hole, giving a  $\gamma$ -ray burst. The problem with this may be that there is little reason for the delay between supernova and  $\gamma$ -ray burst to be even approximately constant, which in turn makes it hard to understand why the iron shell should be about a light day across. Third, the lines have thus far been identified as iron lines, and in cases with an independently known redshift that does appear the best in terms of the observed line energy of 7 keV (Piro et al. 1999, 2000). However, a supernova produces primarily nickel, not iron. In figure 1 we show the total abundance of iron, cobalt, and nickel as a function of time since the supernova. Iron does not become the most abundant element until three months after the supernova, and it takes over half a year for it really to dominate.

The other type of model is different than that described above in two respects: the irradiated material is presumed to be closer to the source (e.g., Böttcher (2000)), most likely leftover material from the disrupted star. Also, the irradiation source is long-lived. It could either be the afterglow itself or residual accretion onto the compact remnant of the hypernova. The fact that the line flux and afterglow flux evolve differently with time favors the latter (e.g., in GRB 000214; Antonelli et al. 2000). A slight variation on this is the model by Rees and Mészáros (2000), who assume the compact object emits a relativistic wind, which gives rise to heating and radiation when it hits the disrupted star. This makes little difference, since in both cases the net effect is that the surface of the ejecta produces the line radiation due to bombardment with X rays. In this model, the density of the line emitting material can be much higher, and thus the number of recombination photons per atom is much larger. Since also this model is naturally anisotropic and thus requires fewer photons produced to begin with, much less iron-group material is needed, but enrichment by supernova ejecta still seems required (Böttcher 2000). This model does not require a delay between supernova and  $\gamma$ -ray burst, and thus is more consistent with the observed supernova signatures in  $\gamma$ -ray bursts. However, the lack of delay aggravates the line identification problem: in the first few days the ejecta really are dominated by nickel, yet the line energy as observed is usually more consistent with iron.

While both types of model thus have problems, we feel that the disagreement in timing between the observed signs of supernovae in a few  $\gamma$ -ray bursts and the predictions of the supernova model are very hard to overcome. In this paper, we investigate the possibility of remedying the line energy problem in the context of hypernova models, where we use the

idea from Rees and Mészáros (2000) that we see a line emitted from the walls of a funnel in the progenitor star that has just been created by the burst. The wall is energized by residual emission of energy from the compact object formed during the  $\gamma$ -ray burst.

### 3. Model and calculations

We model the funnel and the scattering and emission within it as follows: the funnel is taken to be a cone with some fixed opening angle,  $\theta_0$  (to be precise,  $\theta_0$  is the angle between the cone axis and the wall). The wall is taken to have a high enough density that the mean free path of photons within the wall material is negligible compared to the cone size, so that all scattering within the wall takes place in a skin layer of negligible depth. Absorption processes are parametrized by assuming a fixed, energy-independent ratio for the scattering to absorption mean free path. Photons are emitted isotropically from a ring on the cone surface some fixed distance from the apex of the funnel. The ratio,  $h_{cone}$ , of the total height of the cone to the emission height is another parameter of the problem.

We use Monte Carlo calculations to compute the photon propagation and energy change. Since the scattering of the photons is by free electrons, the angular information of scattering events must be retained in order to calculate the direction of the outgoing photon and to determine the photon energy loss. The calculations are undertaken as follows. A photon is emitted on the surface of the cone, and its direction is chosen randomly in spherical coordinates  $(\phi, \cos \theta)$ . In this coordinate system,  $\theta = 0$  points directly out of the cone and  $\theta = \pi$  points directly down;  $\phi = 0$  points to the axis of the cone. Depending on the direction the photon may either escape entirely, cross the cone and enter the wall at a new location, or enter the wall at its current location. One condition to describe the escape of the photon is

$$\theta < \theta_0. \quad (1)$$

The condition which describes whether the photon will cross the cone is given by

$$\cos \phi > \tan \theta_0 / \tan \theta. \quad (2)$$

If the photon crosses the cone, the change in height of the photon is given by

$$\frac{\Delta h}{h} = 2 \frac{(\cos \phi + \tan \theta_0 / \tan \theta)}{\tan \theta / \tan \theta_0 - \tan \theta_0 / \tan \theta}. \quad (3)$$

If the new height,  $h_{new} = h + \Delta h$  is greater than the total height of the cone, then the photon escapes. If  $h_{new} < h_{cone}$  the photon will enter the cone wall at the new point and we then need the direction of the photon at the cone coordinates of the new point. The angle

$\theta$  is unchanged at this new position. However, the coordinate system has rotated in  $\phi$ , since  $\phi = 0$  always points back to the center of the cone. The new  $\phi$  is given by

$$\phi_{new} = \pi - \arcsin \left[ \frac{\sin \phi}{1 + \frac{\Delta h}{h}} \right]. \quad (4)$$

If the photon enters the wall, for bookkeeping purposes, rotation matrices are used to describe its direction in coordinates where  $\theta = 0$  parallel to the edge of the wall. For convenience, we will refer to these as the wall coordinates. The wall coordinates are given in terms of the cone coordinates as

$$\cos \theta_w = -\cos \phi \sin \theta \sin \theta_0 + \cos \theta \cos \theta_0; \quad (5)$$

$$\sin \phi_w = \sin \phi \sin \theta / \sin \theta_w. \quad (6)$$

Inside the wall, the photon scatters off an electron at a distance randomly determined by the photon mean free path  $\lambda_{scatt}$ , such that the probability of the photon traveling a distance  $d$  before scattering is  $P_{scatt} \propto \exp(-d/\lambda_{scatt})$ . Given this distance  $d$ , the photon has a probability of being absorbed of  $P_{abs} = 1 - \exp(-d/\lambda_{abs})$ . In our calculations, we take  $\lambda_{abs} = n\lambda_{scatt}$  and we examine several different values of  $n$ , as discussed in the next section. Rather than throw away photons which fail the absorption test, we track a photon intensity which begins as  $I = 1$  and is multiplied by the absorption probability after each scattering. Every photon which has not escaped the cone by the time its intensity has diminished to less than a percent is discarded in our calculations. For  $\lambda_{abs} \approx 100$ , these photons have typically diminished in energy so they are between 0.8–1.2 keV. If the photon is not absorbed, we calculate the distance from the edge of the wall at which the scattering occurs, using  $d$  and the two angles in the wall coordinate system,  $x = d \sin \theta_w \cos \phi_w$ .

The scattered photon has a direction relative to the photon before scattering which is chosen randomly according to the Thomson cross section  $\sigma_{Th} \propto 1 + \cos^2 \theta_{out}$ , where  $\theta_{out}$  is the angle of the photon coming out of the scattering event relative to the angle of the photon going into the scattering event  $\theta_w$ . The energy of the photon is degraded according to this angle:  $E + \delta E = E/[1 + (E/m_e c^2)(1 - \cos \theta_{out})]$ , where  $m_e$  is the mass of the electron.

In order to determine whether the photon can escape the wall,  $\theta_{out}$  and  $\phi_{out}$  must be converted to the wall coordinate system:

$$\cos \theta_{wout} = -\sin \theta_w \sin \theta_{out} \cos \phi_{out} + \cos \theta_w \cos \theta_{out} \quad (7)$$

$$\sin \phi_{wout} = (\sin \theta_w \cos \phi_{out} \cos \theta_w \sin \theta_{out}$$

$$\begin{aligned} & + \cos \phi_w \sin \phi_{out} \sin \theta_{out} \\ & + \sin \phi_w \sin \theta_w \cos \theta_{out}) / \sin \theta_{wout} \end{aligned} \quad (8)$$

Once the new photon direction is described in the wall coordinate system, we determine whether it escapes the wall. We again randomly choose a distance traveled,  $d$ , according to the mean free path. We update the distance from the edge of the wall to be  $x + \Delta x$ , where  $\Delta x = d \sin \theta_{wout} \cos \phi_{wout}$ . We test to see if the photon's path has taken it outside the wall. If not, we continue to allow the photon to scatter in the wall until it leaves the wall or its intensity has decreased to less than one percent. Once the photon leaves the wall we use rotation matrices to describe it again in the cone coordinate system. It then either escapes the cone entirely or crosses to a new point on the cone and enters the wall at a new height, calculated as starting with Eq. 3, with the exception that the initial path length into the wall,  $d$ , is not chosen randomly. It is the path length from the photon's exit, diminished by the amount needed to exit the wall.

In summary, the photon bounces around in the cone and in the walls of the cone until it either escapes or its intensity becomes negligible. The intensities and energies of all escaping photons are recorded and used to generate the line profiles discussed in the next section.

## 4. Results

We present line profiles calculated from various cone heights and opening angles and absorption mean free paths. We make contact with observation by convolving our profiles with Gaussian functions and adding power law spectra. We also examine the effect of the finite lifetime of various isotopes produced in a supernova-like explosion. In particular we look at the time rate of change of nickel, cobalt and iron abundances and the effect on the line profiles.

Before presenting the results of the Monte Carlo simulations, it is worth pointing out that there is an analytic expression for the average number of scatterings a photon will have on the way out of the cone, in a certain limiting case. If the photon does not wander into the wall and only stays on the surface, there is no absorption, and the funnel is infinite, the average number of bounces that a photon will have on its way out of the funnel is,

$$\bar{N} = (1 + \cos \theta_0) / (1 - \cos \theta_0), \quad (9)$$

where  $\theta_0$  is again the opening angle of the cone. One can see that for small cone opening angles the average number of scatterings is quite large. For example for  $\theta_0 = 10^\circ$ , the average number of bounces before escape is 130, approximately half of which are bounces ‘backward’,

i.e., bounces which do not result in cone crossings. Reducing the cone height to  $h_{cone} = 2$ , but keeping the rest of the simplifications, this number is reduced to 27. This is due to the long tail in the distribution of number of scatterings; e.g., in the infinite cone limit with  $\theta_0 = 10^\circ$ , the median number of scatterings is 89 (for a height of 2, the median is 16), whereas the mode is 0 for any opening angle.

These long tails are also present in all of the line profiles presented here, which are calculated by the method described in the previous section. For example in Fig. 2 extended line profiles occur for all the cone heights studied. This figure shows results for cone heights of  $h_{cone} = 2$  and  $h_{cone} = 10$ . The line photons are always emitted from a height of 1, so the cone heights should be interpreted as ratios. Both figures plot results for cone opening angles of  $\theta_0 = \pi/16$ ,  $\theta_0 = \pi/8$  and  $\theta_0 = \pi/4$ . One can see that increasing the opening angle has an effect which is similar to decreasing the height of the cone, and this is demonstrated in Figure 3. The tail length is strongly influenced by the absorption mean free path, since the tail contains photons which have scattered many times. Fig. 4 shows cases where the mean free path for absorption has been reduced to  $\lambda_{abs} = 10\lambda_{scatt}$ , and  $\lambda_{abs} = 2\lambda_{scatt}$ . Since the ratio is mostly a function of temperature, with colder material being more absorbing, this illustrates the effect of changing the wall from hot to cold; for X-ray photons, the wall retains considerable absorption opacity until the temperature reaches the keV range. Mostly we use a hot wall, with  $\lambda_{abs} = 100\lambda_{scatt}$ , because a radiation bath that suffices to ionize iron and nickel all the way to a hydrogen-like ion will also reduce the X-ray absorption opacity to very much below that of a cold gas.

The curves which have the initial photons emitted from or close to the surface of the wall have several features. There is an initial spike at the energy of the original line. These are all of the photons which escape immediately without any scatterings. There is also a pair of peaks separated by about  $\Delta E/E = 2E/m_e c^2$ , with the higher-energy one almost coincident with the escape spike. The lower energy peak comes primarily from the photons which scatter once in the opposite direction of the opening angle and then scatter back, but also partially from twice scattered photons. Fig. 5 shows the decomposition of one of the line profiles into one, two, three, and four times scattered photons. The completely unscattered photons are not plotted as a separate curve, since they simply comprise the initial spike. The effect of the angular dependence of the Thomson cross section is very clearly seen in the once scattered curve. This is very similar to the energies shown in Illarionov et al. (1979) of photons scattered off free electrons, but without any geometrical constraints such as in our study.

We also show the lines convolved with Gaussians which mimic the spectral resolutions of the CCD and the High Resolution Transmission Grating (HETG) of the Chandra X-



ray observatory. For the former, we use a full width at half maximum of 0.1 keV and for the latter a full width at half maximum of 0.0033 keV; these values are appropriate near  $E = 4$  keV, where the lines are seen in our (observer) frame. A power-law spectrum with photon index  $-2.2$  is added to the profiles with ten times the number of counts (between 2 and 10 keV) as in the peak of the line, to mimic the background against which the line in the GRB 991216 spectrum is seen. We define the ‘peak’ as the area within twice the full width at half the initial peak height maximum, after convolution. We have also given our line profiles a redshift of  $z = 1$ , since recently detected lines have occurred at roughly this redshift (Piro et al. 2000). In figure 6 we show the effect of the CCD resolution and of the high resolution grating. The lower resolution smears out most of the features of the line near the peak, but the large scattering wing remains clearly visible.

The coarser CCD resolution however, is adequate for studying the time variation of the signal due to decay of the nickel and cobalt isotopes. In Figure 7 we show examples of these time profiles. Here we have used the results of supernova nucleosynthesis abundance calculations of Woosley & Weaver (1995) as initial conditions (Model S40C), and allowed the unstable isotopes to decay, keeping track of all abundances. Most of the change in the line profiles we present is due to the decay of the  $A = 56$  isotopes of nickel, cobalt and iron. We have used line energies of 8 keV for nickel, 7.4 keV for cobalt, and 6.9 keV for iron. Nickel-56 has a relatively short half life of 6.1 days as compared with Cobalt-56, which has a half life of 78.8 days. In figure 7 we show line profiles at 0.3, 1, 3, 10, and 100 days after the explosion. Even shortly after the explosion, the line profile clearly changes on a time scale of days as Nickel-56 decays to Cobalt-56. At later times, one can clearly see the build-up of the iron abundance on time scales of months.

One further curious point should be noted here: the decay of Nickel-56 is almost exclusively by electron capture. This means that fully ionized Nickel-56 has a decay time many orders of magnitude longer than than neutral Nickel-56! The wall material we see is dominated by fully ionized material, and therefore in principle Nickel could dominate the observed emission even longer. Hydrogen-like Nickel-56 will decay only half as fast as neutral Nickel-56, because only one of the capturable K shell electrons is present. Cobalt-56 decays by both electron capture and positron emission, so it will decay in fully ionized state, but 5 times more slowly than normal. Of course, the ionized part of the wall is very thin and thus contains almost no mass. Therefore, any amount of mixing in the material that makes up the funnel will cause a given atom to spend little time in the fully ionized state, and thus the influence of ionization on the decay rate may be small in practice.

#### 4.1. Connection with real sources

Thus far, we have phrased our results in terms of the minimal number of (mostly dimensionless) parameters and thus kept them general. However, we do primarily have the physical setting of a hypernova-GRB in mind, so we briefly sketch a set of numbers to which our model applies, that represent the likely situation in the aftermath of a GRB powered by a collapsing massive star. It is very like the situation sketched by Rees and Mészáros 2000. In order to have the required  $10^{52}$  photons/s in the observed line, we require perhaps  $10^{53}$  ph/s emitted above the ionization threshold. This in turn implies an X-ray luminosity of  $L_X \sim 10^{45}\beta$  erg/s, where  $\beta > 1$  converts the ionizing luminosity into the total source luminosity. This is well in excess of the Eddington luminosity of a stellar-mass black hole, and thus cannot be emitted by the vicinity of the black hole in photons. This poses no problems to the model because, as suggested by Rees and Mészáros 2000, it can be emitted as a particle wind and converted to X rays in shocks near the funnel wall.

If we take  $h \sim 2$ , and take the total funnel size to be of order the initial size of the star ( $2 \times 10^{11}$  cm), then the line photons will be primarily generated at  $r \sim 10^{11}$  cm. This implies a very high local X-ray flux at the reprocessing site:  $F_X = 10^{22}\beta$  erg cm $^{-2}$ s $^{-1}$ . Under such circumstances, the temperature in the funnel wall will be set by ionization/recombination physics to a value a few times less than the ionization threshold energy, which in this case is about  $10^8$  K. The density in the funnel wall will be set by the fact that the wall gas pressure must balance the impinging radiation pressure, which implies  $n_e = 10^{19}\beta$  cm $^{-3}$ . With this, we can assess the great importance of radiative ionization in the wall: the ionization parameter,  $\xi = L/nr^2 = 10^4$ , indicating even iron-group elements are largely ionized. It could even be so high that Thompson scattering becomes important: the scattering mean free path is only  $10^5$  cm, illustrating that the wall is indeed very thin. Within this layer, the electron temperature could become dominated by scattering, and set to the Compton temperature,  $kT_C \sim E_\gamma/4$ , which is likely of order 1 keV for a typical X-ray spectrum. (Note that whether it is set by Compton scattering or ionization balance, the temperature is well below the line energy, justifying our approximation of a cold wall, in which only Compton downscattering of the photons is important. Also, the thermal width of any iron-group lines will be of order 1 eV, negligible relative to the scattering width.)

The high degree of ionization of nickel means that the mean free path due to the tiny fraction of hydrogenlike Ni atoms can be orders of magnitude smaller than the scattering mean free path. This implies (Fig. 9) that the line may easily be scattered to a width that effectively makes it invisible. Thus, the transient nature of the observed lines, as well as their total absence in some GRBs, might well be due to too high an ionizing flux instead of a too low one.

## 5. Discussion

Our study of the influence of the funnel in hypernovae on emerging X-ray lines shows that the shape of the lines is very strongly affected by scattering off the funnel walls. This is true even if the funnel has an opening angle as large as 45 degrees and the line photons are produced halfway between the bottom and top of the funnel. Quite generically, the lines can be broadened to 0.5-1 keV FWHM, and their centers shifted down in energy by up to 1 keV before they become too wide to recognize as lines. An important characteristic is that the line remains fairly sharp on the blue side, with a broad red wing being the main reason for the increased width and line-center shift. If the lines are shifted down even further, then they tend to become so smeared out that they may escape detection against a background power-law spectrum from the source.

In Figure 8 we show an example of how a line may appear to become redshifted due to Compton scattering. In this figure, 8 keV nickel lines were emitted at an optical depth of 2 and  $\lambda_{scatt} = 10\lambda_{abs}$ , from a cone with  $h = 10$  and  $\theta_0 = \pi/8$ . The peak of this line occurs at around 7 keV, which happens to be the same energy as iron  $K\alpha$  lines. We see that absorption effects, both as the photons make their way out of the wall and also on the tail of the distribution conspire to create a peak about 1 keV below the original line energy.

The shape of the lines in the case of perfect scattering (i.e., no photons are lost by absorption) is mostly set by the direct-escape probability from the emission point. Since this probability reflects a combination of the funnel opening angle and the funnel height relative to the emission point, it follows that those two parameters are very difficult to disentangle from realistic data. The observed line wing is quite sensitive to absorption, though: as the importance of absorption is increased, most photons never escape the funnel. Since the escaping ones are always those which have scattered few times, their energies have not changed very much. As is illustrated by figures 2–5, the lines always have very extended wings in the perfect-scattering case, even if the cone is wide and the escape probability high: there is always a significant number of photons that scatter many times. The only exception to this is absorption, which ensures that no photons scatter many times. Therefore, narrowness of the line core due to wide funnels can be distinguished from narrowness due to absorption by inspecting the red wing of the line.

A most interesting feature of the profiles is the structure near the original line energy: the escape peak, a sign of unscattered flux, and two or three bumps near it that represent the 1–3 times scattered photons. The bumps are very clear signs of a Compton scattering origin of the line, and can only be seen with grating resolution. Unfortunately, their presence is not guaranteed, as can be seen in figure 9. Rees and Mészáros (2000) showed that close to the compact object, the required X-ray flux is so large that the ionized surface layer of the

funnel becomes optically thick to Thomson scattering (since the atomic edge cross section for nickel or iron is more than 100 times the Thomson cross section, this requires extreme ionizing fluxes). This means that a typical line photon is not created at the wall surface, but at a few scattering optical depths into the wall. As a result, the number of photons that escape with few scatterings becomes minimal very quickly, removing the typical signatures of Compton scattering. (Note that especially for narrow funnels, the escape direction from the cone is nearly perpendicular to the wall normal, so even a small optical depth into the wall reduces the direct-escape probability to nearly zero.)

Another way in which the line shape can be affected is by the angle of exit. Especially the flux that escapes the funnel from near the top, at an angle greater than the cone opening angle,  $\theta_0$ , has a markedly different spectrum than the total flux: the direct escape spike and the back-scatter spike (i.e., the red spike of once-scattered photons plus the peak of the twice-scattered ones) are markedly smaller (figure 10).

## 6. Conclusion

We have shown that the funnel geometry associated with a hypernova naturally produces some features of the emission lines observed in afterglows. Especially the large width of the line seen in GRB 991216 is a natural result of the large scattering wings induced by repeated Compton recoils as a photon bounces around many times in the funnel prior to escape. Therefore, it is not necessary to invoke very high velocities of dense gas clumps or shells to explain the wide lines. At the same time, this causes the center energy of the line to be lowered by large amounts, depending on the funnel depth and opening angle. Widths of 0.5–1 keV, as observed, can be obtained reasonably well. For significantly greater widths the line becomes unrecognizable, however.

The far red wing of the line provides a diagnostic of the relative importance of scattering and absorption opacities in the funnel wall and thus, of the temperature of the wall upon which this ratio chiefly depends. At grating resolutions, one can furthermore recognize sharp spikes in the line due to the photons that have scattered 0–2 times prior to escape. The magnitude of these lines is a measure of the escape probability from the bottom of the funnel (a combination of the opening angle and the depth).

The shape of the lines is further affected by the composition of the ejecta. Contrary to most earlier papers on the subject, the ejecta cannot predominantly emit iron lines unless they are older than half a year. Any younger ejecta are dominated by nickel and/or cobalt. The only other time at which the ejecta are strongly dominated by only one iron-group

element is the first 1–2 days, but then the dominant element is nickel, of which the  $K\alpha$  line is at 8 keV. The discrepancy between this and the observed line energy of 7 keV can be explained by Compton downscattering.

In short, we feel that there is evidence in the lines of scattering origin in a hypernova funnel. Future high-resolution spectra (with long exposure times) will easily confirm or deny this proposition. If confirmed, the shape of the lines provides direct diagnostics of the properties of the hypernova remnants in  $\gamma$ -ray bursts.

GCM and GEB are supported by the U.S. Department of Energy under grant DE-FG02-88ER40388. RAMJW is supported in part by NASA (award no. 21098).

## REFERENCES

- Amati, L., et al. 2000, *Science* 290, 953
- Antonelli, L. A., et al. 2000, *ApJ* 545, L39
- Böttcher, M. 2000, *ApJ* 539, 102
- Bloom, J. S., Kulkarni, S. R., & Djorgovski, S. G. 2000, *AJ* submitted, (astro
- Bloom, J. S., et al. 1999a, *Nature* 401, 453
- Bloom, J. S., Sigurdsson, S., & Pols, O. R. 1999b, *MNRAS* 305, 763
- Bulik, T., Belczynski, K., & Zbijewski, W. 1999, *A&AS* 138, 483
- Costa, E., et al. 1997, *Nature* 387, 783
- Eichler, D., Livio, M., Piran, T., & Schramm, D. N. 1989, *Nature* 340, 126
- Frail, D. A., Kulkarni, S. R., Nicastro, L., Feroci, M., & Taylor, G. B. 1997, *Nature* 389, 261
- Fruchter, A. S. 2001, *Proc. Rome GRB meeting*, October 2000
- Galama, T., et al. 2000, *ApJ* 536, 185
- Galama, T. J., et al. 1998, *Nature* 395, 670
- Galama, T. J. & Wijers, R. A. M. J. 2001, *ApJ*, 549, L209
- Janka, H-Th., Eberl, T., Ruffert, M. and Fryer, C., 1999, *ApJ* 527, L39

- Illarionov, A., Kallman, T., McCray, R., & Ross, R. 1979, *ApJ* 228, 279
- Kommers, J. M., Lewin, W. H. G., Kouveliotou, C., van Paradijs, J., Pendleton, G. N., Meegan, C. A., & Fishman, G. J. 2000, *ApJ* 533, 696
- Kouveliotou, C., Meegan, C. A., Fishman, G. J., Bhat, N. P., Briggs, M. S., Koshut, T. M., Paciesas, W. S., & Pendleton, G. N. 1993, *ApJ* 413, L101
- Krumholz, M. R., Thorsett, S. E., & Harrison, F. A. 1998, *ApJ* 506, L81
- Mészáros, P. & Rees, M. J. 1997, *ApJ* 476, 232
- Metzger, M. R., Djorgovski, S. G., Kulkarni, S. R., Steidel, C. C., Adelberger, K. L., Frail, D. A., Costa, E., & Frontera, F. 1997, *Nature* 387, 879
- Mochkovitch, R., Hernanz, M., Isern, J., & Martin, X. 1993, *Nature* 361, 236
- Paczyński, B. 1998, *ApJ* 494, L45
- Piran, T. 1999, *Phys. Rep.* 314, 575
- Piro, L., et al. 1999, *ApJ* 514, L73
- Piro, L., et al. 2000, *Science* 290, 955
- Rees, M. J. & Mészáros, P. 1992, *MNRAS* 258, L41
- Rees, M. J. & Mészáros, P. 2000, *ApJ* 545, L73
- Reichart, D. E. 1999, *ApJ* 521, L111
- Salmonson, J. D., Wilson, J. R. and G. J. Mathews 2001, *ApJ* 553, 471
- Schmidt, M. 2001, *ApJ* 552, 36
- Totani, T. 1997, *ApJ* 486, L71
- van Paradijs, J., et al. 1997, *Nature* 386, 686
- van Paradijs, J., Kouveliotou, C., & Wijers, R. A. M. J. 2000, *ARA&A* 38, 381
- Vietri, M., Ghisellini, G., Lazzati, D., Fiore, F., & Stella, L. 2001, *ApJ* 550, L43
- Wijers, R. A. M. J., Bloom, J. S., Bagla, J. S., & Natarajan, P. 1998, *MNRAS* 294, L13
- Wijers, R. A. M. J., Rees, M. J., & Mészáros, P. 1997, *MNRAS* 288, L51

Woosley, S. E. 1993, ApJ 405, 273

Woosley, S. E. & Weaver, T. A. 1995, ApJS 101, 181

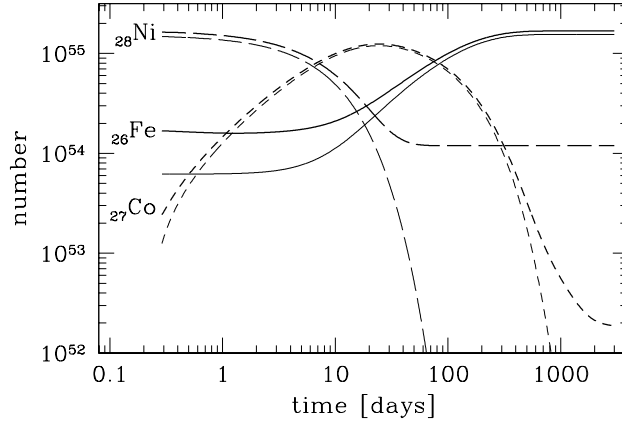


Fig. 1.— Abundances of nickel, cobalt, and iron, as a function of time since the supernova for a  $40M_{\odot}$  star (model S40C,  $16M_{\odot}$  He core) as modeled by Woosley & Weaver (1995). The thick lines give the sum over all isotopes, the thin ones represent only the  $A = 56$  isotope of each.



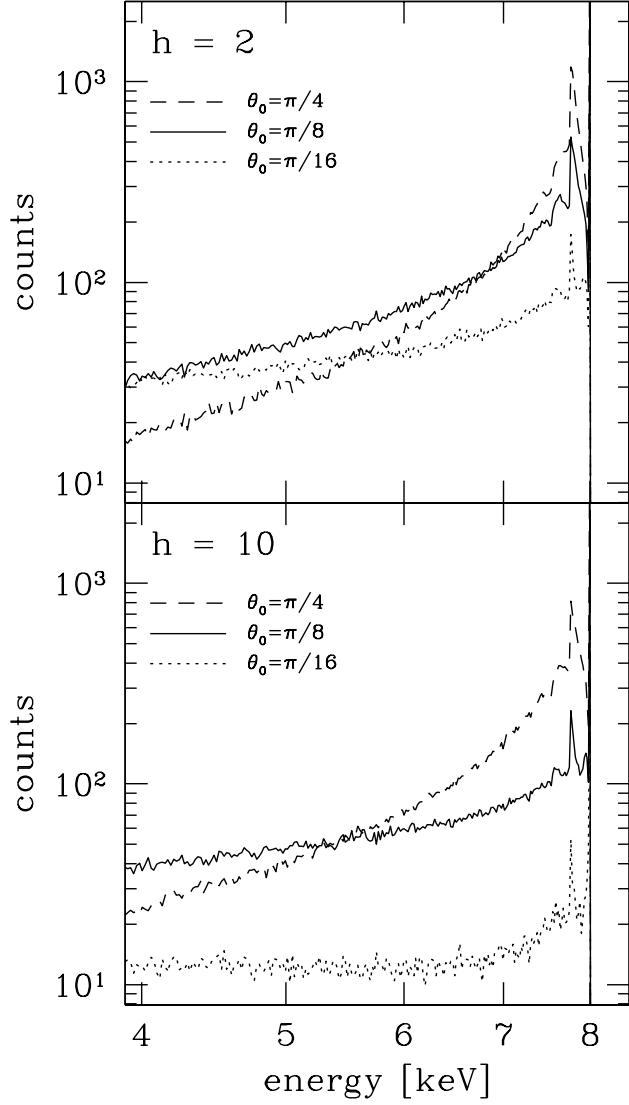


Fig. 2.— Line profiles for cone heights of 2 (top) and 10 (bottom). Photons of energy 8 keV are emitted at height 1. In each panel we show the effect of decreasing opening angle:  $\theta_0 = \pi/4$  (dashed),  $\theta_0 = \pi/8$  (solid), and  $\theta_0 = \pi/16$  (dotted). As the opening angle decreases, the peak of few-times scattered photons near 8 keV decreases, and the low-energy tail becomes flatter. The depression is stronger for greater height at all opening angles.

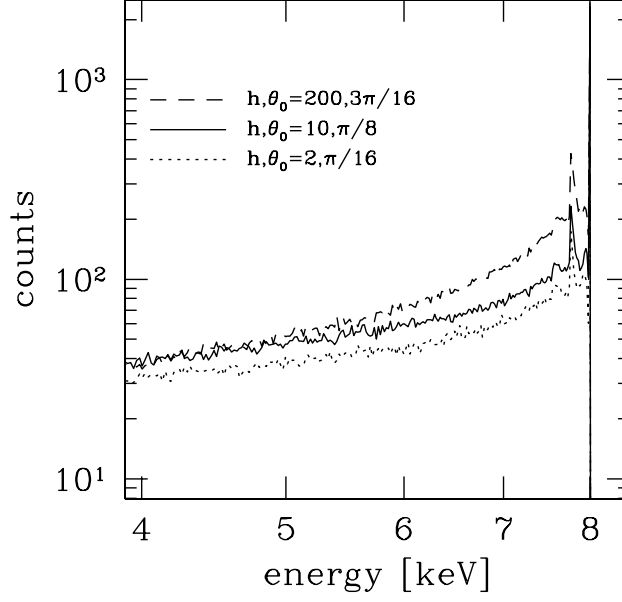


Fig. 3.— Increasing the opening angle of the cone has an effect which is very similar to decreasing the height, as illustrated by the similarity of three cases: the top curve has  $(h, \theta_0) = (200, 3\pi/16)$ , the middle one has  $(10, \pi/8)$ , and the bottom one  $(2, \pi/16)$ .

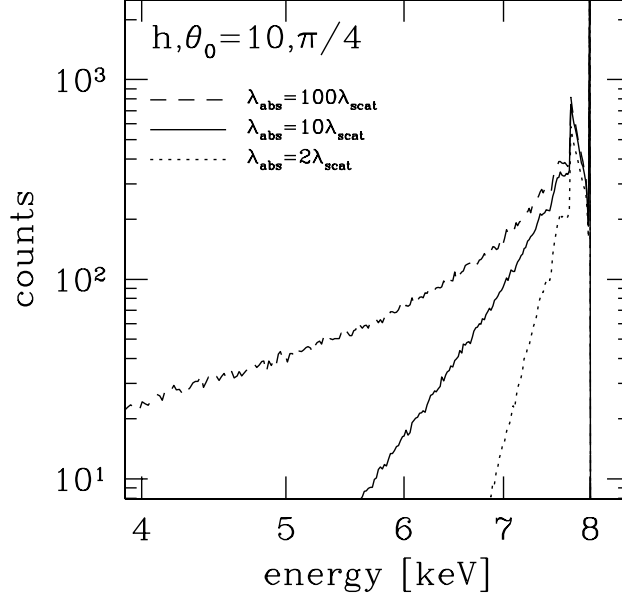


Fig. 4.— The effect of increasing the relative importance of photon absorption. The top curve is made with  $\lambda_{abs} = 100\lambda_{scatt}$ , the middle one with  $\lambda_{abs} = 10\lambda_{scatt}$ , and the bottom one with  $\lambda_{abs} = 2\lambda_{scatt}$ . The opening angle of the cone is  $\pi/4$  and the height is 10.

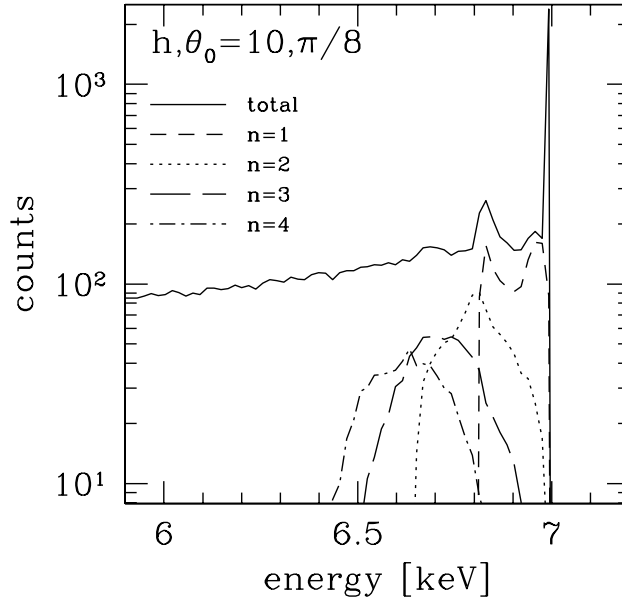


Fig. 5.— Decomposition of a line profile with a cone height of 10, and opening angle of  $\pi/8$  into photons emitted with one, two, three and four bounces. These are shown as the lower curves with number of bounces increasing from right to left. The overall line profile is shown as the solid line.

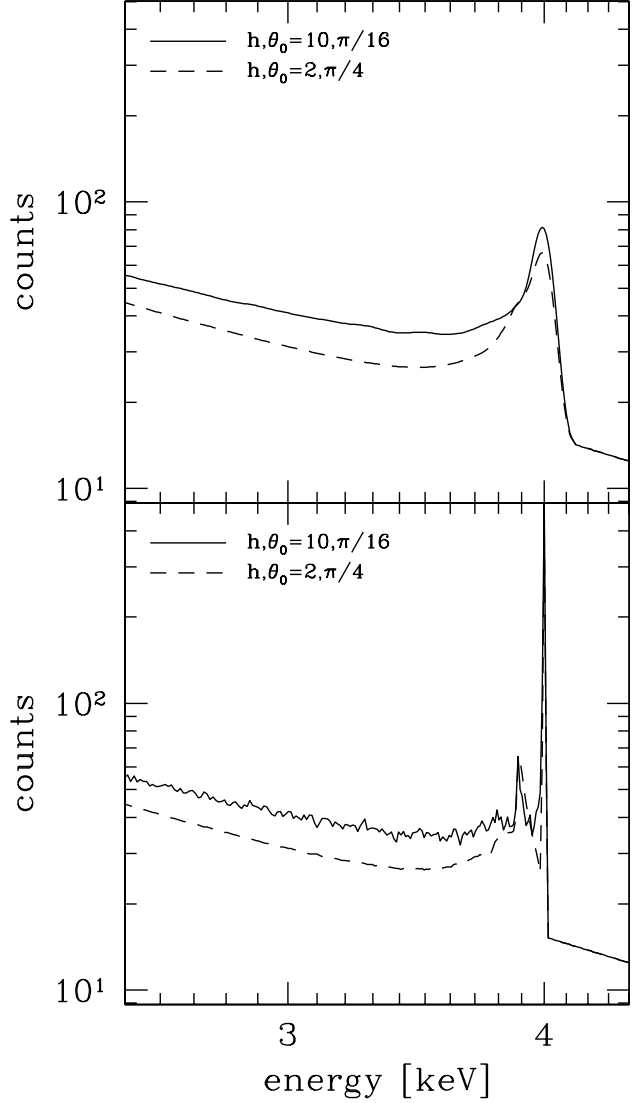


Fig. 6.— Line profiles redshifted to  $z = 1$  and convolved with a Gaussian to simulate detector resolution. A power-law spectrum has also been added with ten times as many counts as in the narrow part of the line, so the overall spectrum resembles that of the observed case of GRB 991216 (Piro et al. 2000). The lower line shows the profile for a height of 2 and an angle of  $\pi/4$ . The upper line shows the profile for a height of 10 and an angle of  $\pi/16$ . The top panel is for a resolution of 0.1 keV around the line energy, mimicking the Chandra CCD, and the bottom panel mimics the Chandra HETG with a resolution of 0.003.

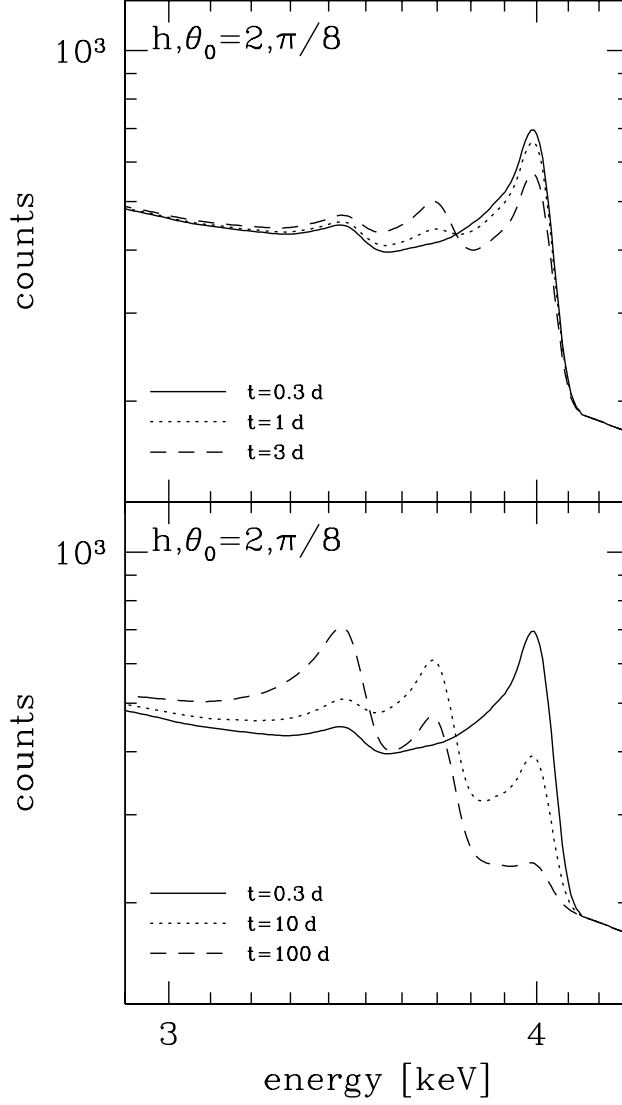


Fig. 7.— The evolution of the redshifted line profile at CCD resolution (0.1 keV) as it decays from primarily nickel isotopes to iron, by way of cobalt. In the top panel we show the line after 0.3 days (solid), 1 day (dotted), and 3 days (dashed). The bottom panel is for delays of 0.3 (solid), 10 (dotted), and 100 (dashed) days. In this figure the funnel height is 2 and the cone angle is  $\pi/8$ .

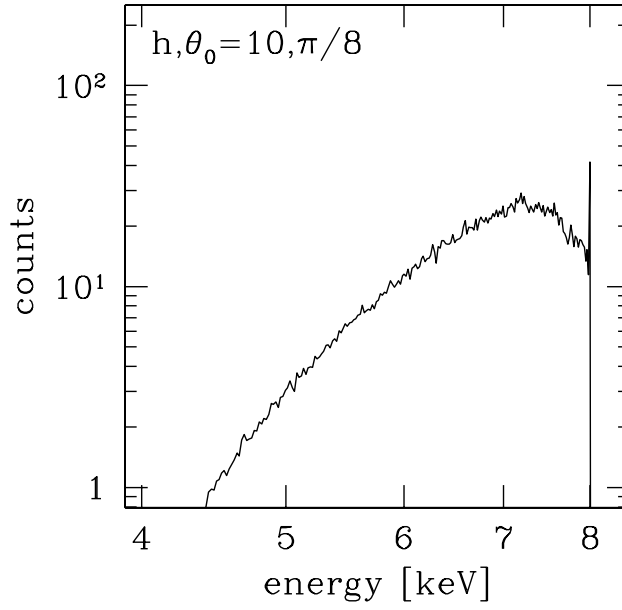


Fig. 8.— The shift of an 8 keV line to 7 keV in a cone with  $h = 10$  and  $\theta_0 = \pi/8$ . The photons were emitted at an optical depth of 2 and the ratio of scattering to absorption is 10. The shift of the line peak is due to the combined effect of starting at finite optical depth, which depresses the blue side, and absorption of the tail, which depresses the red side.

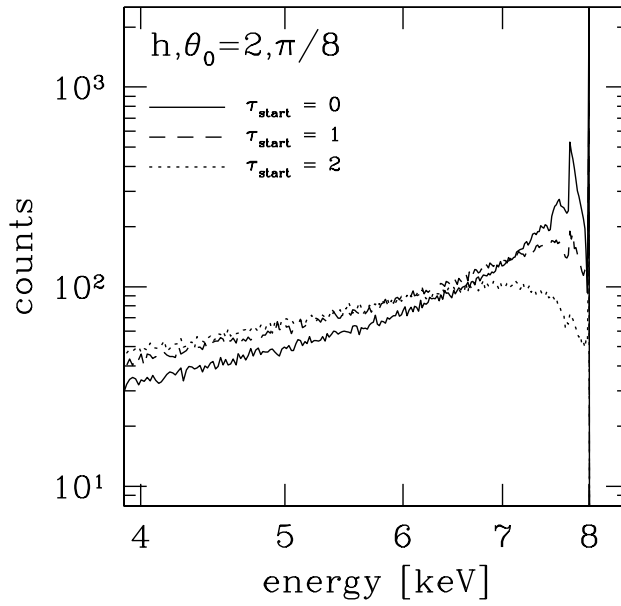


Fig. 9.— The effect of emission of the line photons at finite scattering optical depth. The solid curve is for photons initially emitted at the surface of the wall. The dashed line is for photons emitted at an optical depth of 1, and the dotted line is for those emitted at an optical depth of 2. The initial spike heights for the three curves are in a ratio of 22:4:1. The plot was made for an opening angle of  $\pi/8$  and a cone height of 2.



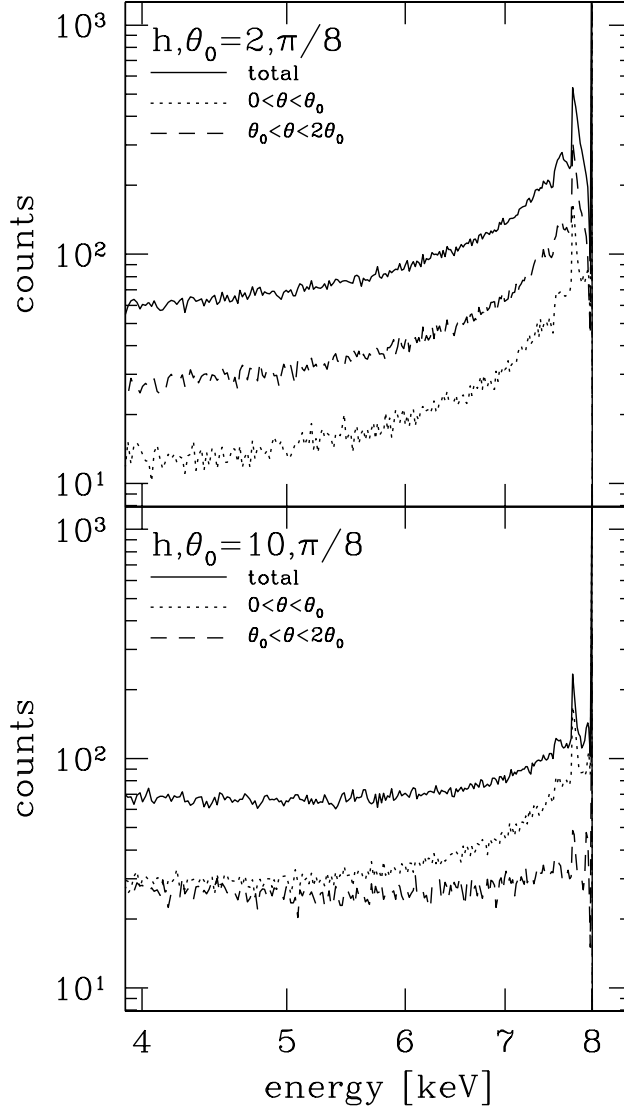


Fig. 10.— The variation in intensity and shape of the line profile with emission angle (or the observer viewing angle relative to the cone axis), for an opening angle of  $\pi/8$  and cone heights of 2 (top) and 10 (bottom). The top curve (solid) in both panels is the sum over all emission angles. The dashed curve represents the photons emitted with angles between  $\theta_0$  and  $2\theta_0$ , and the dotted one those emitted between between 0 and  $\theta_0$ . Note how the intensities of the on-axis and off-axis components are reversed between the shallow cone (top) and the deep cone (bottom).